Rainfall and DSD Parameters Comparison between Micro Rain Radar, Two-Dimensional Video and Parsivel^2 Disdrometers, and S-Band Dual-Polarization Radar

ELISA ADIROSI AND LUCA BALDINI

Institute of Atmospheric Sciences and Climate, CNR, Rome, Italy

ALI TOKAY

Joint Center for Earth Systems Technology, University of Maryland, Baltimore County, Baltimore, and NASA Goddard Space Flight Center, Greenbelt, Maryland

(Manuscript received 15 May 2019, in final form 19 December 2019)

ABSTRACT

A well-designed deployment of well-maintained surface instruments as well as abundant rainfall provided an excellent dataset with which to evaluate the Micro Rain Radar (MRR) performance for estimating raindrop size distribution (DSD) and its integral rainfall parameters with respect to the consolidated devices during the Iowa Flood Studies (IFloodS) field campaign. The MRR was collocated with two-dimensional video disdrometer (2DVD) and Autonomous Parsivel^2 Unit (APU) at three different sites located at 5–70-km distances from the National Aeronautics and Space Administration's S-band dual-polarization Doppler radar (NPOL). A comparative study between MRR, 2DVD, APU, and NPOL was conducted including all rainy minutes as well as minutes of stratiform rain and convective rain. Considering 2DVD as a primary reference, a good agreement was evident for reflectivity between MRR's lowest reliable height and 2DVD with an absolute bias of less than 2 dB even in convective rain except for one site. For rainfall rate, the percent absolute bias between MRR and 2DVD ranged between 25% and 35% in stratiform rain and about 10% higher in convective rain. Agreement for mean mass-weighted raindrop diameter was good (bias less than 0.1 mm), whereas MRR overestimated the normalized intercept parameter of the gamma DSD [mean bias among the three sites was -0.13 log(mm^{-1} m^{-3})]. The agreement between MRR and APU was slightly worse than the one between MRR and 2DVD. When the horizontal and differential reflectivities of NPOL were compared with the ones derived from the MRR DSD resampled within the radar volume, we found an absolute bias of approximately 3 and 0.4 dB, respectively.

1. Introduction

Knowledge of the vertical structure of precipitation is essential for the quantitative precipitation estimation (QPE) from spaceborne and ground-based weather radar. For spaceborne radars such as the National Aeronautics and Space Administration (NASA) Global Precipitation Measurement (GPM) mission Dual-Frequency Precipitation Radar, the vertical profile of precipitation is retrieved down to the lowest uncluttered bin, which ranges from 250 m at nadir to approximately 3 km at the edges (Kubota et al. 2014) and can be affected by terrain complexity. Ground-based weather radar estimates precipitation in a resolution volume located at an altitude that is dependent on the radar beam elevation angle, the beamwidth, and the distance from the radar. In that regard, the radar coverage is very limited below 1 km above ground, even in relatively flat regions. Maddox et al. (2002, their Fig. 5b) show the limited radar coverage for the contiguous United States at 1 km AGL. The variation in vertical profile of reflectivity (VPR) is well recognized as a source of uncertainty in radar QPE (Zhang et al. 2016). The problem is more severe in orographically complex regions where blockage forces the use of sweeps at higher elevation angles.

The observational evidence for the variability in VPR near the ground is best suited to either a range–height indicator mode of scanning radars (Schuur et al. 2012) or vertically pointing radars (Williams 2002; Giangrande et al. 2012). These observations are available during field campaigns or at long-term ground observation sites

Corresponding author: Luca Baldini, l.baldini@isac.cnr.it

DOI: 10.1175/JTECH-D-19-0085.1

equipped with research weather radars such as those funded through the Department of Energy Atmospheric Radiation Measurement program and the NASA GPM Ground Validation program in the United States. Among the vertically pointing radars, Micro Rain Radar (MRR) has been widely used for precipitation studies because it comes with built-in raindrop size distribution (DSD) retrieval software (Peters et al. 2005). Its low cost, low maintenance and commercial availability make it quite attractive for research organizations around the globe. It has been used to determine the diurnal features of precipitation in Ecuador (Bendix et al. 2006); compare brightband features between coastal and mountain sites in South Korea (Cha et al. 2009); determine the vertical variability of the relationship between reflectivity and rain rate (Tokay et al. 2009); characterize seasonal and orographic precipitation features in the United States (Prat and Barros 2010); investigate the vertical profile of rain in India (Das et al. 2010; Kirankumar and Kunhikrishnan 2013), Spain (Fraile et al. 2015), and East China (Wen et al. 2016); investigate the impact of precipitation variability within a measurement volume on the performance of dual-polarization rain algorithms in Italy (Gorgucci and Baldini 2015); and calibrate operational weather radar in Germany (Frech et al. 2017). A number of these studies include either rain gauge or a disdrometer and comparisons between the lowest reliable MRR gate and surface instrument have been done for reflectivity, rain rate and rain accumulation. As noted by Frech et al. (2017), MRR data fill the gap between the measurements at the ground and aloft by a scanning radar. In that regard, MRR has a potential to be used by operational agencies. A network of MRRs at selected sites can enhance the capability of precipitation mapping of nationwide weather radar networks.

Micro Rain Radar, manufactured by Meteorologische Messtechnik GmbH (Metek), is a K-band, low-power frequency-modulated continuous-wave profiler. It measures Doppler spectra from which vertical profiles of DSD are retrieved from near the ground to 1–6 km, depending on the range resolution. Currently, two versions of MRR are commercially available: MRR-2, which has 32 gates, and the newer MRR-PRO, which has up to 254 range gates with a minimum height resolution of 10 m. The minimum averaging intervals have also been improved from 10 to 1 s in MRR-PRO.

The accuracy of the MRR retrievals is influenced by a number of factors, including Mie scattering, microwave attenuation, variation in fall velocity and shape of raindrops, vertical wind, and turbulence (Chen et al. 2015). The MRR manufacturer's algorithm is developed for liquid precipitation, and the output is given as "raw," "processed," and "averaged" data, depending on the level of processing applied. Although some of the factors listed above are addressed in both processed and averaged data, MRR is considered to be less reliable in heavy convective rain because of the presence of a larger number of large drops and vertical wind. Tridon et al. (2011) recognized the velocity folding (aliasing) in MRR Doppler spectra due to strong vertical wind and offered automatic detection and correction, which led to better DSD retrieval. Adirosi et al. (2016) presented an alternative methodology for improved MRR-based DSD retrieval in the presence of vertical wind, which is adopted in this study. MRR is also considered less reliable in snow due to the higher sensitivity of snowflakes to turbulence, high dependency of the size–fall velocity relationship to the flake habit and differences in backscattering cross section of the frozen particles to Mie scattering (Kneifel et al. 2011). Maahn and Kollias (2012) improved MRR snow measurements through postprocessing Doppler spectra and verified their results through comparing reflectivity, Doppler velocity and spectrum width with a collocated 35.2 GHz vertically pointing cloud radar.

MRR has been an integral component of the ground instrumentation deployed during the GPM Ground Validation (GV) field campaigns and is included in the System for Integrating Multiplatform Data to Build the Atmospheric Column (SIMBA) precipitation observation fusion framework (Wingo et al. 2018). Among the GPM GV field campaigns, the Iowa Flooding Studies (IFloodS) provided a unique dataset for a comparative study including MRR-2. IFloodS was the first integrated hydrologic GPM GV field campaign designed for better understanding of the strengths and limitations of satellite products for hydrological applications (Petersen and Krajewski 2013). Favorable natural conditions led to abundant rainfall, and even local flooding, during the field campaign. A special collection of papers published in the *Journal of Hydrometeorology* is evidence of the richness of the IFloodS dataset. Among them, Seo et al. (2018) compared various radar rainfall estimates with gauges and Chen et al. (2017) focused on improving dual-polarization radar rainfall algorithms using NASA's S-band dual-polarization radar (NPOL) and an Autonomous Parsivel^2 Units (APU) network with respect to different characteristics of the events observed during the campaign. Thurai et al. (2017) developed a weighted algorithm for X-band dual-polarization rainfall estimation using the two-dimensional video disdrometer (2DVD) network, Iowa X-band dual-polarization radar, and the rain gauge network.

In this study, a comprehensive evaluation of MRR performance was carried out by comparing DSD and integral rainfall parameters obtained from MRR raw

data with the corresponding ones calculated from 2DVD and APU observations and the ones derived from NPOL measurements. The comparison with disdrometers was made both at ground level—that is, at the lowest reliable MRR gate—and along the vertical, comparing the disdrometer data at ground with MRR retrievals at different heights to investigate the effect of vertical gradients of precipitation on MRR–disdrometer comparison. The comparison with NPOL was made along the vertical considering coincident bins and measurements during both stratiform and convective rain conditions. To improve the reliability of MRR retrievals in convective rain, the postprocessing of Adirosi et al. (2016) was applied to raw MRR spectra and the results were compared to standard MRR products.

The paper is organized as follows. Section 2 describes the experimental datasets used in this study. Section 3 reports the equations used to compute the DSD and rainfall parameters from disdrometer and MRR raw data. Section 4 gives the equations considered to evaluate the performance of MRR. The DSD and integral products derived from MRR-measured Doppler spectra are validated through comparative study with collocated disdrometers (in section 5) and coincident NPOL measurements (in section 6). Conclusions are given in section 7.

2. Experimental dataset

a. Experimental setup

IFloodS took place in eastern Iowa in April–June 2013. NPOL was located close to Waterloo, Iowa (42.268°N, 92.509°W; Wolff et al. 2015a), and six clusters of disdrometers and rain gauges were deployed approximately along an NPOL azimuth at sites from 5 to 106 km away. In each site, 2DVD (Petersen et al. 2014a) and APU (Petersen et al. 2014b) disdrometers were collocated (interdistance less than 10 m). Three of these sites had two–four APUs nearby (within 10 km), and one site had one additional APU collocated. The APUs recorded from 396 to 539 mm of rainfall in 72 days, evidence of abundant rainfall during IFloodS. Four of the six sites included also an MRR-2 (Petersen et al. 2015) operated at the vertical resolution of 35 m. One MRR did not operate properly. Therefore, this study uses the data from three MRR-2 sites, which were 5, 24, and 69 km from NPOL (Fig. 1 and Table 1). For such sites, collocated were only one 2DVD and one APU. This experimental setup, along with the abundant rainfall recorded, created an ideal dataset for a comparative study to evaluate the performance of MRR.

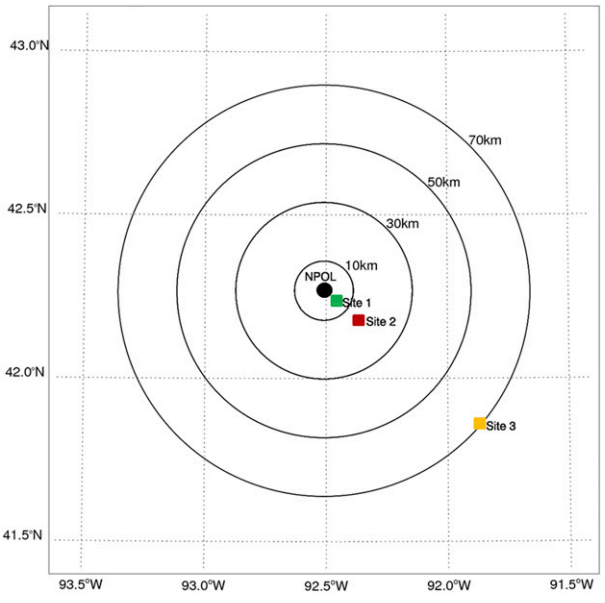

FIG. 1. Instrument location map. At the three sites highlighted by colored squares, data collected by collocated MRR, 2DVD, and APU are available. The black dot indicates the location of the NASA NPOL.

NPOL is a transportable research-grade S-band system; it operated nearly continuously during the IFloodS field campaign. The scanning strategy adopted during IFloodS consisted of plan position indicator (PPI) and range–height indicator (RHI) scans. Two PPI scans provided 360° coverage at 0.67° and 1.39°. Sector PPI and RHI scans aimed to sample particular precipitation structures in depth, while PPI scans at 90° elevation were performed during several events for differential reflectivity Z_{dr} calibration monitoring, depending on the occurrence and location of precipitation echoes. The entire scan cycles that always included the low-elevation PPIs were completed in 1–3 min whenever precipitation was within range of the radar (Wolff et al. 2015b).

The GPM GV office conducted quality control, which may reduce the sample size, especially at short distances due to clutter effects (Pippitt et al. 2015) and was responsible of NPOL calibration. Both engineering and solar calibration were performed for calibration. PPIs at vertical incidences have been used for verification of Z_{dr} calibration that indicated a Z_{dr} bias near 0.0 dB for the entire field campaign. For monitoring Z_h calibration, they applied the self-consistency principle and made comparisons between NPOL and 2DVD. The results of the two techniques were in agreement (D. Marks 2019, personal communication). The relative calibration adjustment (RCA) technique was applied during the field campaign to monitor the relative stability of NPOL calibration (Wolff et al. 2015b). This study uses

TABLE 1. Site locations.

	Lat (°)	Lon (°)	Height (m ASL)	Distance from NPOL (km)	NPOL first elev height (m AGL)	NPOL second elev height (m AGL)
Site 1	42.239	−92.464	283	4.98	71	132
Site 2	42.126	−92.282	284	24.5	340	639
Site 3	41.861	−91.874	258	69.2	1125	1969

PPI data collected at the two lowest elevation angles (0.67° and 1.39°) that include correction for calibration biases. For the IFloodS campaign, the pulse duration of NPOL was 0.8 μs and the pulse repetition frequency was set at 1100 Hz. Data were provided every 1° that correspond to using 72 pulses per sample and with a range resolution of 150 m.

The 2DVD is an optical device using two orthogonal light sheets projected onto an array of 512 discrete photodetectors inside two line-scan cameras to measure, for each single hydrometeor that falls through the device measuring area of nominally $10 \times 10\,\text{cm}^2$, the equivolume drop diameter D, oblateness, and fall velocity (Schönhuber et al. 2007). Its third generation consists of an outdoor measurement unit and an indoor analysis computer. The manufacturer reports that the accuracy of size and vertical velocity is better than 0.17 mm and 4%, respectively, for particles falling at less than $10\,\text{m s}^{-1}$. The underestimation of small drops less than 0.5 mm in diameter is perhaps the main shortcoming of the 2DVD in rain (Thurai and Bringi 2018). This could have a pronounced effect on the accuracy of the intercept parameter of fitted distribution and low moments of size spectrum (Thurai et al. 2017).

The OTT Parsivel^2 (APU) is a laser-based optical disdrometer. It has an optical sensor that produces a horizontal sheet of light (30 mm wide, 1 mm high, and 180 mm long) that is focused on a single photodiode. A hydrometeor that passes through the light sheet reduces the signal amplitude at the photodiode for a certain time, allowing the measurement of the dimension and the fall velocity of the particle. The raw output provided by the manufacturer's software is the number of drops in 32 size and 32 fall velocity categories with variable widths. The underestimation of fall velocity for drops larger than 1 mm and the underestimation of small drops less than 0.7 mm in diameter are the main shortcomings of Parsivel^2 in rain (Tokay et al. 2014). The fall velocity is required to compute the DSD.

b. Data processing

The GPM GV program processed the NPOL data, which include radar measurements such as radar reflectivity factor at horizontal polarization Z_h, differential reflectivity Z_{dr}, and the copolar correlation coefficient ρ_{hv} used in this paper along with radar rain rates computed using three different algorithms, several other radar specific parameters, and derived size distribution parameters (Pippitt et al. 2015). In this study, nonmeteorological echoes were filtered out by including only the radar bins with ρ_{hv} greater than 0.9 and adopting a clutter filter based on the standard deviation of Z_{dr} (Lombardo et al. 2006) computed over a 3×3 pixel box. Boxes with a value outside the 0.09–0.9 dB interval are filtered out.

Considering the disdrometer datasets, a filter criterion (Tokay et al. 2001) was adopted to remove spurious secondary drops and nonmeteorological particles that were collected by APU or 2DVD. The criterion filters out any drops with a measured fall velocity outside the range ±50% of the fall velocity of Atlas et al. (1973) that, in this study, was used also to compute DSD and related parameters. To construct DSD, raw drop-by-drop outputs of 2DVD were stratified in 50 bins with a constant width of 0.2 mm. The bin widths increased with size from 0.1 to 1.0 mm for APU (Tokay et al. 2013). Both 2DVD and APU observations were integrated to 1-min resolution.

The MRR estimates DSD from Doppler spectra. After subtracting the noise level, using calibration constant and range-weighting function, the measured spectral power was converted first to spectral reflectivity density (volume reflectivity: $\text{m}^2\,\text{m}^{-3}$ per unit of velocity) for each Doppler spectral bin. Under the assumption of negligible vertical wind and assuming the relationship between raindrop diameter and terminal fall velocity of Atlas et al. (1973), the spectral reflectivity density with respect to the drop diameter can be obtained and then converted into drop size spectra by dividing by the single particle backscattering cross section of a raindrop (Peters et al. 2005). It should be reiterated that MRR is subject to attenuation and the manufacturer algorithm applies a correction for the attenuation in the processed and averaged data (Peters et al. 2010). The assumption of absence of vertical wind in the DSD retrieval algorithm is not always reliable. Vertical winds can shift MRR Doppler spectra toward lower or higher velocities (which will result in shifting the

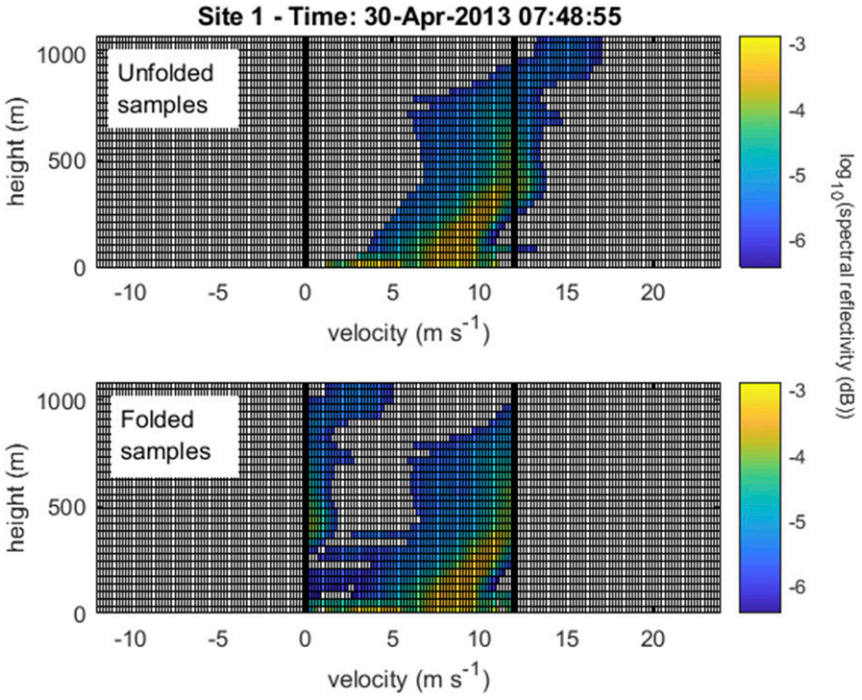

FIG. 2. Example of the unfolding process applied to the MRR spectra: (bottom) an example of samples affected by aliasing and (top) the same samples after the correction. The data shown were collected on 0748 UTC 30 Apr 2013 at site 1.

estimated DSD toward small and large drops, respectively) and, in some cases, can be affected by aliasing. Adirosi et al. (2016), taking advantage of collocated measurements of 2DVD and MRR, suggested a new processing of the MRR raw spectra to improve the reliability of MRR retrievals in the presence of vertical wind. The two major changes in the MRR processing chain are the dealiasing and shifting of the MRR spectra. The dealiasing procedure is applied to each MRR spectrum and is similar to the one proposed by Maahn and Kollias (2012). It consists of considering three adjacent spectra and identifying the peak, lower and upper limits of the triplicated spectrum. The second step consists of shifting each 1-min MRR spectrum by a quantity that is equal to the difference between the characteristic fall velocity computed from the MRR at 105 m above ground level (AGL) and the one obtained from the collocated 2DVD. The present study adopts such postprocessing. Figure 2 shows an example of the application of the unfolding process. Furthermore, before applying the MRR postprocessing, the transfer function used to obtain the spectral reflectivity from the raw spectral power has been calibrated considering the spectral reflectivity reported in the processed MRR data. Hereinafter, the DSD and the corresponding variables obtained after the application of this postprocessing are labeled as ''REP'' and the MRR-averaged data provided by Metek are labeled as ''AVE.''

For the DSD datasets obtained from APU, 2DVD and MRR, the 1-min samples with rain rate R outside $0.1 < R < 300\,\mathrm{mm\,h^{-1}}$ and radar reflectivity factor Z outside $-20 < Z < 55\,\mathrm{dB}Z$ were discarded. The snow days and the MRR profiles with brightband signature were excluded from the dataset. A cross comparison between 2DVD and APU led to eliminating 2 days at two sites.

3. Integral rainfall parameters

The DSD is the base for a number of hydrological and meteorological integral variables including rain rate, radar reflectivity factor, mean mass-weighted raindrop diameter D_{mass}, and intercept parameter of the gamma distribution normalized with respect to the liquid water content N_w that can be expressed as

$$R = 0.6\,10^{-4}\pi\int_{D_{\min}}^{D_{\max}} N(D)D^3 v(D)\,dD \quad (\mathrm{mm\,h^{-1}}), \quad (1)$$

$$Z = \int_{D_{\min}}^{D_{\max}} N(D)D^6\,dD \quad (\mathrm{mm^6\,m^{-3}}), \quad (2)$$

$$D_{\text{mass}} = \frac{\int_{D_{\min}}^{D_{\max}} N(D) D^4 \, dD}{\int_{D_{\min}}^{D_{\max}} N(D) D^3 \, dD} \quad \text{(mm)}, \quad \text{and} \tag{3}$$

$$N_w = \frac{256}{\pi \rho_w} \frac{10^3 \text{LWC}}{D_{\text{mass}}^4} \quad (\text{m}^{-3}\,\text{mm}^{-1}), \tag{4}$$

where $N(D)$ is the DSD; D is the equivolume drop diameter; $v(D)$ is the drop terminal velocity; $D_{\min}$ and $D_{\max}$ are the minimum and maximum drop diameters, respectively; ρ_w is the density of water ($\text{g}\,\text{cm}^{-3}$); and LWC is the liquid water content:

$$\text{LWC} = \frac{\pi 10^{-3}}{6} \rho_w \int_{D_{\min}}^{D_{\max}} N(D) D^3 \, dD \quad (\text{g}\,\text{m}^{-3}). \tag{5}$$

Figure 3 shows the cumulative distributions of the integral variables defined above and estimated from the 2DVD, APU and MRR measurements at three sites during IFloodS, and Table 2 reports their mean and maximum values resulting from the great variety of precipitation events observed during IFloodS [see Chen et al. (2017) and Wolff et al. (2015b) for a meteorological description of single events]. For comparison, the coincident rainy minutes of 2DVD and APU and the first reliable range gate of MRR at 105 m above the ground were considered. Please note that the cumulative distributions of the DSD and rain parameters of REP MRR and AVE MRR were nearly identical due to the minimal contribution of convective profiles in the dataset, and therefore, only REP MRRs are shown. In fact, applying the Thurai et al. (2010) algorithm for convective/stratiform rain classification to the AVE DSDs at 105 m AGL results in just 6%, 4%, and 4.2% of convective rain minutes for sites 1, 2, and 3, respectively. Furthermore, aliasing affects a small number of spectra (less than 5%) and its extension is quite limited. The condition shown in Fig. 2 is rare, and usually the aliasing affects only a few spectral bins. Consequently, considering the whole IFloodS dataset, the Adirosi et al. (2016) postprocessing has a minor impact on the results since it is expected to be more effective for convective profiles.

The cumulative distributions of the four variables computed with Eqs. (1)–(4) show a very good agreement at all sites between APU and 2DVD (Fig. 3). Table 2 reports mean and maximum values of the different variable considered in this study. The mean values of R and Z are lower in 2DVD for the first two sites while the largest differences in mean values were observed at site 3 where the APU R and Z are lower of 18% and 1.2 dB, respectively. The mean values of D_{mass} and $\log_{10} N_w$ are also lower in 2DVD for the first two sites and the maximum difference between 2DVD and APU for the means of D_{mass} and $\log_{10} N_w$ are 0.3 and 0.05 mm, respectively. Note that N_w ranges over nearly four orders of magnitude and is expressed by taking the common logarithm of N_w ($\text{mm}^{-1}\,\text{m}^{-3}$). The cumulative distribution of variables has a different degree of agreement between MRR and disdrometers. The distribution of MRR Z has very good agreement with the distributions from 2DVD and APU at sites 1 and 3, but Z is shifted toward lower values for MRR, resulting in a difference of 1.7 dB in mean for site 2. The maximum Z values are drastically lower in MRR than in disdrometers. At site 2, the difference in maximum Z is nearly 9 dB. This is related to the difficulty in determining large drop sizes from Doppler spectra for the MRR. The large drops have a pronounced effect on Z, especially in heavy rain. The mean R of MRR is lower than that of 2DVD for all sites, but the differences are significantly high (35%) at site 2 and low (4%) at site 1. The mean D_{mass} of MRR is lower at all three sites, but the differences are always less than 0.1 mm, showing good agreement. Good agreement is shown also for the other DSD parameter, with at most the mean $\log_{10} N_w$ of REP MRR, 0.25 higher than that of 2DVD at site 1.

The level of agreement between MRR and disdrometers in terms of distribution of variables is linked to the sensitivity of variables to a particular DSD regime. For instance, N_w is sensitive to the number of small drops, and the larger values of N_w of MRR are therefore linked to the overestimation of small drops with respect to the disdrometers. Given the small differences between Z, R, D_{mass} and N_w estimated from the AVE MRR and the REP MRR datasets, in the following sections of this paper we consider only the REP data. If not explicitly written, MRR data means "REP MRR data." However, each time that the two datasets present distinct behaviors we will report and discuss it.

4. Statistics for the evaluation of instrument performances

Four different rainfall statistics were employed to compare the integral variables listed above. Bias and absolute bias (abs bias) are the most meaningful statistics for Z, D_{mass}, and $\log_{10} N_w$, and the difference in R is often referred to as a percentage. Percent bias and percent absolute bias are therefore the leading statistics for R. The rainfall statistics are computed as follows:

$$\text{bias} = \frac{\sum X_i - Y}{N}, \tag{6}$$

$$\text{abs bias} = \frac{\sum |X_i - Y_i|}{N}, \tag{7}$$

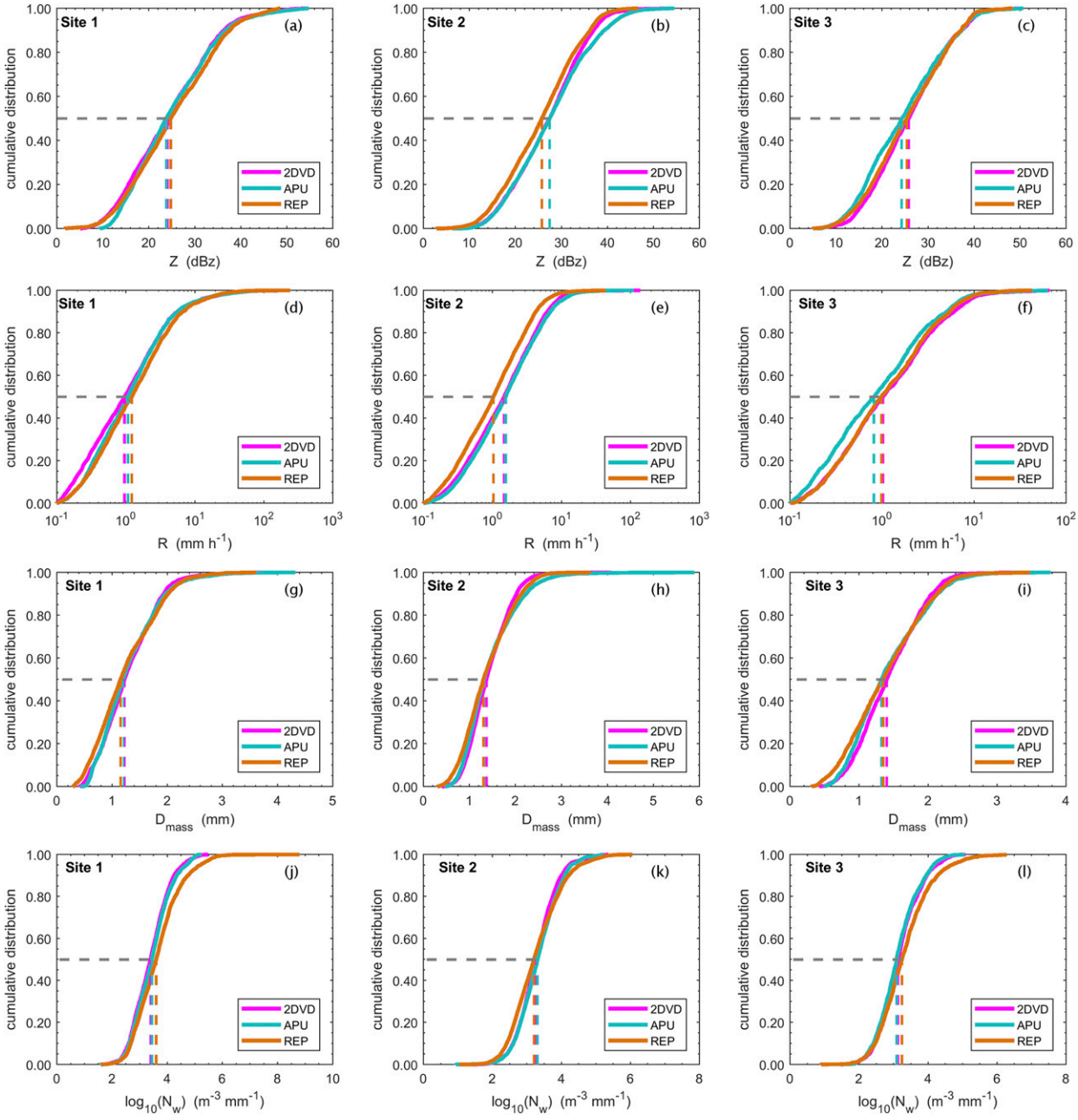

FIG. 3. CDFs of (a)–(c) Z, (d)–(f) R, (g)–(i) D_{mass}, and (j)–(l) $\log_{10}N_w$ for the three sites. Distributions of these variables are obtained from DSDs estimated from measurements collected by 2DVDs (magenta lines), APUs (green lines), and MRRs at 105-m height (brown lines).

$$\text{percent bias} = \frac{\sum X_i - Y_i}{\sum X_i}, \quad \text{and} \tag{8}$$

$$\text{percent abs bias} = \frac{\sum |X_i - Y_i|}{\sum X_i}. \tag{9}$$

In Eqs. (6)–(9), X is the reference and Y is the estimator. Since this study compares MRR with APU, 2DVD, and NPOL, MRR is always the estimator. Negative values of bias or percent bias indicate an overestimation of MRR with respect to the reference instrument. The bias alone cannot express the level of agreement. The absolute bias is also referred to as absolute error when one of the instruments is taken as a reference, and is therefore the key statistic for judging the agreement. A similar argument is true for the percent statistics. The correlation coefficient is used to determine to what extent two variables can be considered

TABLE 2. Mean and maximum values of Z, R, D_{mass}, and $\log_{10}N_w$ obtained at the three different sites from the DSD estimated from data collected by 2DVD, APU, and MRR at 105 m considering both the REP and the AVE data.

	Site 1		Site 2		Site 3	
	Mean	Max	Mean	Max	Mean	Max
Z 2DVD (dBZ)	24.46	54.25	27.05	54.20	25.99	49.82
Z APU (dBZ)	25.04	54.81	27.70	54.60	24.78	50.76
Z REP MRR at 105 m (dBZ)	25.30	48.59	25.50	46.76	25.58	48.44
Z AVE MRR at 105 m (dBZ)	25.15	48.22	25.33	45.67	25.37	47.69
R 2DVD (mm h^{-1})	2.99	161.42	2.69	139.54	2.44	66.16
R APU (mm h^{-1})	3.06	148.74	2.93	112.02	2.00	63.60
R REP MRR at 105 m (mm h^{-1})	3.17	242.01	1.85	44.04	2.13	43.21
R AVE MRR at 105 m (mm h^{-1})	2.87	251.07	1.74	48.34	1.98	38.78
D_{mass} 2DVD (mm)	1.29	3.91	1.42	4.09	1.44	3.33
D_{mass} APU (mm)	1.30	4.33	1.45	5.90	1.42	3.78
D_{mass} REP MRR at 105 m (mm)	1.25	3.61	1.38	3.64	1.38	3.48
D_{mass} AVE MRR at 105 m (mm)	1.23	3.84	1.37	3.98	1.37	3.29
$\text{Log}_{10}N_w$ 2DVD	3.41	5.49	3.29	5.37	3.18	5.09
$\text{Log}_{10}N_w$ APU	3.46	5.25	3.33	5.23	3.13	5.07
$\text{Log}_{10}N_w$ REP MRR at 105 m	3.66	8.80	3.27	6.07	3.32	6.28
$\text{Log}_{10}N_w$ AVE MRR at 105 m	3.61	6.85	3.26	6.46	3.30	5.71

as linearly related. However, it cannot evaluate the level of agreement between the variables. Rather, the coupled high correlation and low bias indicate a high level of agreement.

5. MRR–disdrometer comparisons

In this section, the performance of MRR is evaluated with respect to the two available disdrometer types. Only the coincident minutes collected by MRR, 2DVD, and APU were considered. This allowed us to correctly evaluate the comparisons of MRR with 2DVD and APU since otherwise results can be affected by the different samples considered.

a. DSD comparisons

Figures 4a, 4d, and 4g show 1-h stratiform DSDs collected at the three sites. The agreement among 2DVD, APU and MRR in terms of midsize drops ($1 < D < 3$ mm) is very good. For the small drop ($D < 1$ mm) regime, the MRR DSD increases with decreasing drop size. In contrast, the 2DVD and APU DSD decreases with decreasing drop size, showing downward concavity. It is historically difficult to determine the drop concentration accurately for the small drop regime. Thurai and Bringi (2018) showed a good agreement in DSD between the 2DVD and Meteorological Particle Spectrometer (MPS) at sizes between 1 and 2 mm in diameter. The MPS, sensitive to the drops down to 50 μm, showed concave upward shape in DSD. For the large drop ($D > 3$ mm) regime, the MRR has an intrinsic upper limit of 5.03 mm, whereas the 2DVD and APU can detect drops up to 10 mm. For stratiform rain, the DSD agreement is good between the three sensors except at site 2, where APU counted more drops at sizes of 3–4 mm in diameter (Fig. 4d).

Figure 4 highlights also the DSD differences in terms of rain rate (Fig. 4b,e,h,k),and reflectivity (Fig. 4c,f,i,l) obtained from the 1-h DSDs for each size bin. For rain rate, the peak of the distribution is located between 0.8 and 2 mm; therefore, these drop diameters have the highest contribution during stratiform rain (Figs. 4b,e,h). The size range of highest contribution expands to approximately 3.6 mm in convective rain (Fig. 4k). For reflectivity, the peak contribution was from the drops between 0.8 and 3 mm in diameter in stratiform rain (Figs. 4c,f,i). For convective rain, the peak contribution to reflectivity shifted toward larger drops ranging from 1.2 mm to the maximum drop diameter in DSD (Fig. 4l).

The mass-weighted drop diameter is a result of drop concentration at small, midsize, and large drop size regimes [see Eq. (3)]. The presence of a large number of small drops in MRR DSD (see, e.g., Figs. 4a,d, and g) shifts D_{mass} toward a smaller value, while the presence of large drops in convective 2DVD DSD (see, e.g., Fig. 4j) shifts D_{mass} toward a larger value. The intercept parameter of the normalized gamma function, on the other hand, is sensitive to the drop concentration, which is driven by the number of small drops. Therefore, N_W is expected to be larger in MRR DSDs. It should be noted that the concave upward shape of DSD was not always observed in MRR DSD (not shown). In these cases, MRR-derived N_W should have a smaller value and D_{mass} should shift toward a larger value.

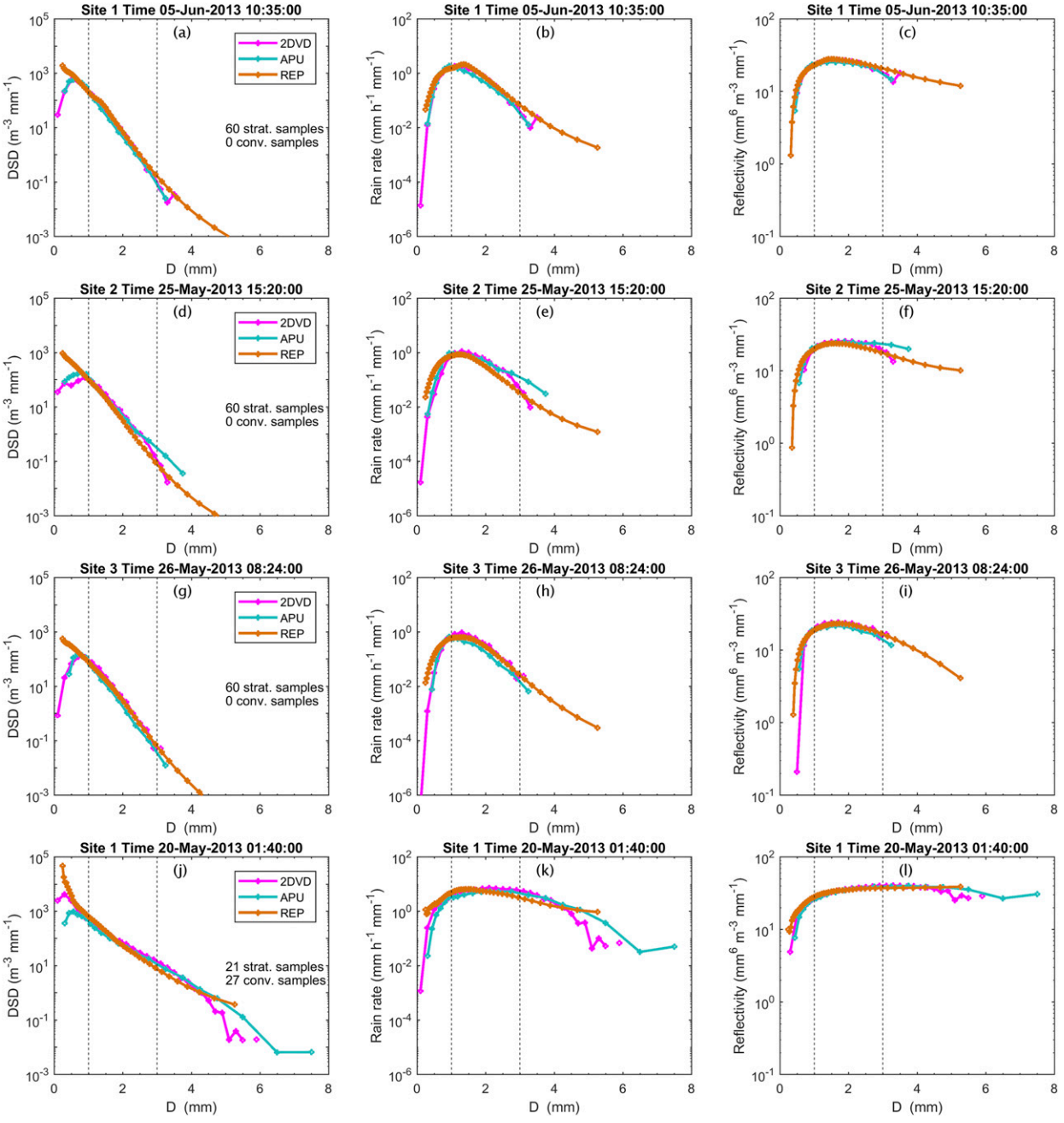

FIG. 4. Examples of the 1-h stratiform DSDs (the time in the plot title indicates the beginning of the hour considered) collected by APU, 2DVD, and REP MRR at 105 m AGL at sites (a) 1, (d) 2, and (g) 3, along with (j) an example of the 1-h DSD with a relatively high number of convective minutes collected by APU, 2DVD, and REP MRR at 105 m AGL at site 1 on 20 May 2013; the corresponding values of (b),(e),(h),(k) rain rate and (c),(f),(i),(l) Z for each size bin obtained from the DSDs shown in the respective left panels. Vertical dashed lines represent the 1- and 3-mm drop diameters.

b. MRR–2DVD comparison

Figure 5 depicts the two-dimensional histograms of the two integral rainfall (Z and R) and two DSD (D_{mass} and $\log_{10}N_w$) variables derived from 2DVD and REP MRR data at 105 m AGL for all of the coincident rainy minutes. Note that, considering a mean drop fall velocity of 5 m s^{-1}, the precipitation sampled at 105 m AGL takes 21 s to reach the ground. Since we are considering 1-min samples, no delay correction was applied. A good agreement between 2DVD and MRR is evident for all four variables for all sites, with an exception of an MRR

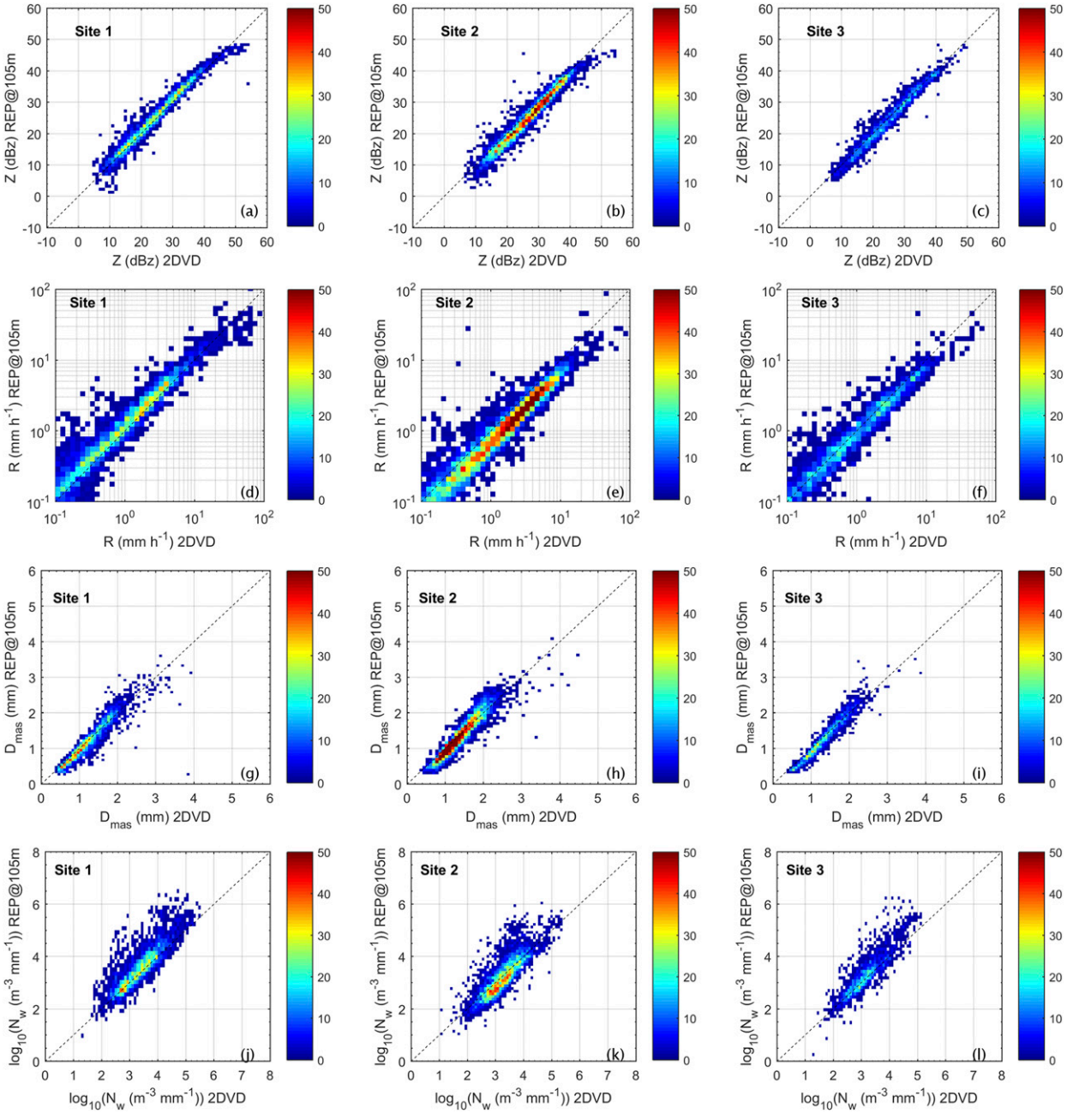

FIG. 5. The 2D histogram between (a)–(c) Z, (d)–(f) R, (g)–(i) D_{mass}, and (j)–(l) $\log_{10}N_w$ obtained from 1-min DSD collected by collocated 2DVD (x axis) and MRR (y axis) at the three selected sites. Variables obtained from REP MRR DSD are shown.

underestimation of Z and R for site 2. The latter can be due to instrumental issues. The dispersion of the data along the 1:1 line is a qualitative measure of agreement between the two variables. Ideally, one seeks a minimum dispersion equally distributed on both sides of such line, with the peak concentration of the data along the line. Indeed, the dispersion was minimal for Z for all three sites, but peak concentration slightly leaned toward the 2DVD measurements at site 2, raising a question of a possible calibration error in MRR (Figs. 5a–c). The dispersion is large for R for all three sites, but the peak concentration leans toward the 2DVD for sites 2 and 3 only (Figs. 5d–f). For the DSD parameters, the dispersion was relatively larger for $\log_{10}N_w$ in contrast to D_{mass}, which has its peak concentration along the 1:1 line (Figs. 5g–i). The peak concentration leans toward MRR for $\log_{10}N_w$ for sites 1 and 3 (Figs. 5j–l).

TABLE 3. Performance of the comparison of 2DVD-based rainfall and DSD parameters and the corresponding ones obtained from REP MRR DSDs at 105 m AGL for three different conditions: all coincident rainy minutes, stratiform rain, and convective rain. Here, corr indicates the correlation coefficient.

	Z (dBZ)			R (mm h^{-1})			D_{mass} (mm)			$\text{Log}_{10}[N_w$ (mm^{-1} m^{-3})]		
	Bias	Abs bias	Corr	Bias	Abs bias	Corr	Bias	Abs bias	Corr	Bias	Abs bias	Corr
2DVD vs REP MRR at 105 m—all minutes (no. of samples: 2759, 4694, 1877 for sites 1, 2 and 3, respectively)												
Site 1	−0.83	1.54	0.977	−4.8%	35.5%	0.745	0.05	0.14	0.937	−0.24	0.34	0.840
Site 2	1.56	1.97	0.972	31.5%	36.7%	0.830	0.04	0.15	0.936	0.01	0.30	0.834
Site 3	0.43	1.50	0.976	11.5%	28.0%	0.880	0.06	0.14	0.961	−0.17	0.29	0.878
2DVD vs REP MRR at 105 m—stratiform minutes (no. of samples: 2546, 4336, 1723 for sites 1, 2 and 3, respectively)												
Site 1	−0.92	1.54	0.973	−21.6%	30.3%	0.919	0.05	0.13	0.943	−0.26	0.35	0.852
Site 2	1.54	1.98	0.967	29.4%	34.7%	0.887	0.05	0.14	0.938	−0.01	0.30	0.832
Site 3	0.49	1.51	0.971	4.9%	24.8%	0.919	0.07	0.13	0.960	−0.19	0.30	0.884
2DVD vs REP MRR at 105 m—convective minutes (no. of samples: 147, 185, 94 for sites 1, 2 and 3, respectively)												
Site 1	0.79	1.72	0.828	13.8%	40.9%	0.503	0.07	0.26	0.629	−0.04	0.32	0.556
Site 2	2.26	2.36	0.842	38.0%	45.1%	0.695	0.06	0.26	0.688	0.14	0.30	0.813
Site 3	1.01	1.58	0.776	24.6%	36.2%	0.737	−0.01	0.17	0.804	0.11	0.22	0.849

Table 3 shows the bias and absolute bias for Z, R, D_{mass}, and $\log_{10}N_w$. The analysis was conducted for 1) all coincident rainy minutes, 2) stratiform rain and 3) convective rain. The coincident samples of stratiform rain were distinguished from those of convective rain applying the Thurai et al. (2010) algorithm to the 2DVD data. Although the algorithm classifies the rainy samples as convective, stratiform and transition, this study considers only the first two categories. The sum of the number of convective and stratiform minutes therefore differs from the total number of samples reported in Table 3. The samples of convective rain are 5.5% or less of the samples of stratiform rain, and the statistics in Table 3 for all and for stratiform rain are therefore very close each other. Recall that the MRR-derived integral rain and DSD parameters are based on Doppler velocity spectra assuming zero vertical air velocity. Vertical air motion in stratiform rain is much less than that in convective rain; therefore, the samples of stratiform rain should be considered as the optimum dataset for evaluating the MRR performance.

The statistics in Table 3 reflect that D_{mass} is well retrieved from MRR with low absolute biases and high correlation coefficients. The bias is 0.07 mm or less and the absolute bias is 0.14 mm or less in stratiform rain. Low bias and absolute bias are obtained also for Z except for site 2, where bias exceeds 1.0 dB and absolute bias is ~2 dB in stratiform rain. This result is consistent with Tokay et al. (2009), who compared MRR-derived (at 175 m above the ground level) and impact-type Joss–Waldvogel disdrometer-calculated Z and found a bias within 2 dB for the majority of the events. Frech et al. (2017) more recently compared MRR-based reflectivity at 650 m AGL with the reflectivity obtained at ground level by a Thies disdrometer, obtaining a bias for $15 < Z < 35$ dB between 0.1 and 0.3 dB and a mean absolute deviation (MAD) between 2.2 and 2.9 dB. The agreement between MRR-derived and 2DVD-calculated R is relatively low, with absolute bias ranging from 24% to 34% in stratiform rain. The bias itself was large, 29.4% at site 2 and −21.6% at site 1. The negative bias indicates an overestimation by MRR, which is not the case in convective rain at the same site. The very few samples of convective rain have a significant role in R, lowering the correlations and differentiating the overall statistics from the statistics in stratiform rain. N_w is sensitive to the number of drops, which is dominated by the small drops. Given the fact that MRR DSD diverges from 2DVD DSD at the small drop regime the most, it is not surprising to have large absolute bias in $\log_{10}N_w$ in all three sites. Sites 1 and 3 have noticeably large negative bias, likely due to abundant small drops in MRR DSD for stratiform rain (Figs. 4a,d,g). The bias of $\log_{10}N_w$ is negative but close to zero for site 1 and is positive for sites 2 and 3 in convective rain. Considering all of the coincident rainy minutes, MRR overestimates R at site 1 and underestimates R for sites 2 and 3. The overestimation of R at site 1 increases considering only the stratiform samples. The underestimation for site 2 is larger (percent bias of 31.5% for all rainy minutes) than the ones of sites 1 and 3, as also reiterated for reflectivity as shown in Fig. 5b. MRR-based R estimations are always smaller than the ones of 2DVD during convective rain, and positive values of bias for all the three sites were obtained.

The results discussed above refer to the REP MRR dataset. Results obtained using the AVE MRR dataset are similar but with some noticeable differences. Actually, the Adirosi et al. (2016) processing reduces the dispersion of data along the 1:1 line, resulting in lower

TABLE 4. Performance of the comparison of 2DVD-based rainfall and DSD parameters and the corresponding ones obtained from AVE MRR DSDs at 105 m AGL for convective rain minutes (number of samples: 146, 180, and 92 for sites 1, 2 and 3, respectively).

	Z (dBZ)			R (mm h^{-1})			D_{mass} (mm)			$\text{Log}_{10}[N_w$ (mm^{-1} m^{-3})]		
	Bias	Abs bias	Corr	Bias	Abs bias	Corr	Bias	Abs bias	Corr	Bias	Abs bias	Corr
Site 1	3.22	4.29	0.529	30.9%	48.0%	0.498	0.38	0.49	0.386	−0.15	0.37	0.668
Site 2	4.31	4.60	0.415	53.8%	56.6%	0.664	0.21	0.40	0.328	0.14	0.34	0.759
Site 3	3.07	3.58	0.375	40.8%	45.4%	0.688	0.17	0.33	0.307	0.05	0.27	0.686

values of absolute bias and percent absolute bias (not shown), particularly for convective rain (Table 4). Table 4 shows the statistics for Z, R, D_{mass}, and $\log_{10}N_w$ obtained from AVE MRR and 2DVD data in convective rain. Both biases and absolute biases are larger when AVE MRR is employed.

Comparison of the 2DVD-based variables obtained at the ground with the MRR-based variables estimated at different heights provides unique information on the vertical variability of precipitation and on the time–height ambiguity between the radar and the disdrometer measurements. The setup of IFloodS allows evaluation of precipitation variability within the first kilometer above the ground, given that the maximum height for the MRR measurements was set to 1085 m AGL. The precipitation sampled by MRR at 1085 m AGL takes more than 3 min to reach the ground, assuming a mean fall velocity of 5 m s^{-1}. However, since we are interested in the characterization of the instantaneous precipitation profile, we did not apply any time delay correction between MRR observations at different heights and surface observations. Therefore, the results presented in the following do not refer only to instrumental differences, but include also the time–height ambiguity effects. Figure 6 shows the statistics in Eqs. (6)–(9) for Z, R, D_{mass}, and $\log_{10}N_w$ obtained by comparing 2DVD and REP MRR data at the different range gates. Recall that the first reliable MRR range gate is centered at 105 m AGL. The absolute bias increases and the correlation decreases with height, but the magnitude of the decrement or increment varies depending on variables considered (Figs. 6b,c,e,f,h,i,k,l). Bias itself does not follow a steady increase or decrease trend with height for all parameters, and may shift its position from positive to negative values or vice versa (Figs. 6a,d,g,j).

The increase in both sampling volume of MRR and time–height ambiguity with height is the main cause for the larger absolute bias and lower correlation at higher altitudes. The trend of absolute bias of Z along the vertical was slightly different for the three sites (Fig. 6b). The maximum differences in absolute bias can be observed at the lowest and the highest gates. The absolute bias of Z at the lowest gate is 2 dB at site 2, 0.5 dB higher than at the other sites, and at the highest gate (1085 m) is 4.3 dB at site 3, 0.4 and 0.6 dB higher than at the other two sites. The absolute biases of Z are very close between 200- and 500-m heights between the three sites, and the absolute bias is around 3 dB at 500 m. The bias of Z is very different from one site to another, but trends at sites 1 and 3 are similar (Fig. 6a). For site 1, the bias of Z ranges from −0.82 to 0.50 dB between the lowest and highest range gates, crossing the zero around 385 m AGL. For site 3, it varies between 0.4 and 1.5 dB. The bias of Z at site 2, on the other hand, remains nearly constant with height and is above 2 dB. The correlations of Z decreased from 0.97 at the lowest gate to 0.76 at the highest gate for all three sites (Fig. 6c).

The trend of percent absolute bias of R at sites 2 and 3 is similar up to 600 m AGL (Fig. 6e). The percent absolute bias of R at site 1 is about the same as that at site 2 below 200 m but increases rapidly with height, reaching 80% at 700 m and remaining at the same value above that height. The correlation coefficient of R decreases more rapidly than any other variable, reaching 0.1 at the highest gate, but is about the same between the three sites at a given altitude (Fig. 6f). There are no similarities in the trend of percent bias of R between the three sites (Fig. 6d). The percent bias of R has a decrease at site 2, while both increasing and decreasing trends are evident at different height intervals at site 3. For sites 2 and 3, the percent bias of R is mainly bounded between 10% and 30%, whereas at site 1 it is negative, −5% at the ground, crosses zero one gate above, and remains less than 15% at all other gates.

The absolute bias of D_{mass} increases from 0.14 to 0.30 mm between the lowest and the highest gates at sites 2 and 3 (Fig. 6h). At site 1, the absolute bias of D_{mass} increases at a slower rate, ending up at 0.28 mm at the highest gate. The bias of D_{mass} increases with height at all sites, but the difference between the lowest and the highest gates was the largest at site 2, ranging from 0.05 to 0.18 mm and is the smallest at site 3, ranging from 0.06 to 0.14 mm (Fig. 6g). The correlations of D_{mass} gradually decrease with height at site 3 and at a bit faster rate at sites 1 and 2 (Fig. 6i). The agreement between the devices remains good, with a bias less than 0.2 mm also at the highest range gate. The absolute bias of $\log_{10}N_w$

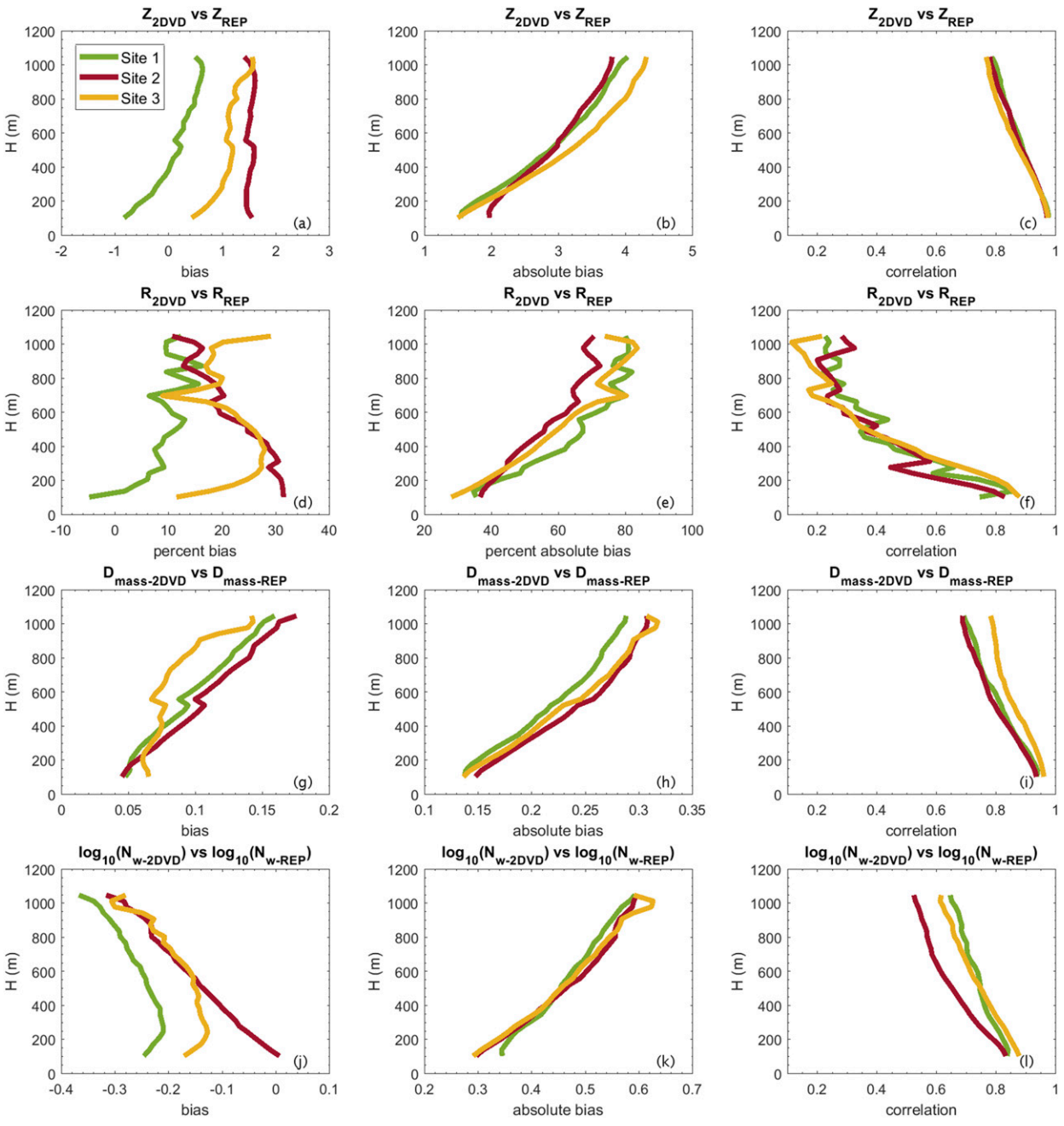

FIG. 6. Comparison of (a)–(c) Z, (d)–(f) R, (g)–(i) D_{mass}, and (j)–(l) N_w from 2DVD and MRR DSD as a function of height for the three sites: (left) the values of bias or percent bias, (center) the values of absolute bias or percent absolute bias, and (right) the values of the correlation coefficient.

increases from 0.3 to 0.6 between the lowest and the highest gates at sites 2 and 3 and the increase in absolute bias was about the same for the other site (Fig. 6k). The bias of $\log_{10}N_w$ decreases with height from nearly zero at the lowest gate to −0.3 at the highest gate at site 2, whereas it first increases from the lowest gate to 245 m and then decreases at a slower rate at sites 1 and 3 (Fig. 6j). The bias is the smallest at all gates at site 1. The correlations of $\log_{10}N_w$ are the lowest and decrease at a relatively faster rate at site 2, ranging from 0.83 to 0.52 between the lowest and the highest gates (Fig. 6l). The magnitude of MRR overestimation of N_w increases with the height. In qualitative terms, we can conclude that, in terms of correlations, the variability of Z, D_{mass}, and

TABLE 5. As Table 3, but for the comparison between APU and MRR (REP).

	Z(dBZ)			R (mm h^{-1})			D_{mass} (mm)			$\text{Log}_{10}[N_w$ (mm^{-1} m^{-3})]		
	Bias	Abs bias	Corr	Bias	Abs bias	Cor	Bias	Abs bias	Cor	Bias	Abs bias	Cor
APU vs REP MRR at 105 m—all minutes (no. of samples: 2717, 4624, 1747 for sites 1, 2 and 3, respectively)												
Site 1	−0.28	1.99	0.959	−3.8%	37.7%	0.718	0.05	0.16	0.921	−0.20	0.33	0.841
Site 2	2.18	2.94	0.932	36.9%	41.1%	0.871	0.07	0.20	0.855	0.06	0.31	0.827
Site 3	−0.79	1.90	0.960	−6.7%	28.0%	0.908	0.04	0.16	0.902	−0.19	0.31	0.817
APU vs REP MRR at 105 m–stratiform minutes (no. of samples: 2565, 4207, 1655 for sites 1, 2 and 3, respectively)												
Site 1	−0.39	1.97	0.952	−18.7%	33.3%	0.901	0.04	0.15	0.924	−0.20	0.33	0.851
Site 2	1.90	2.72	0.921	32.1%	37.1%	0.899	0.04	0.18	0.853	0.06	0.31	0.829
Site 3	−0.91	1.91	0.953	−19.2%	28.4%	0.937	0.03	0.16	0.895	−0.20	0.32	0.820
APU vs REP MRR at 105 m–convective minutes (no. of samples: 120, 261, 47 for sites 1, 2 and 3, respectively)												
Site 1	2.00	2.53	0.827	15.7%	43.6%	0.433	0.27	0.34	0.658	−0.19	0.32	0.570
Site 2	5.56	5.59	0.623	47.4%	50.8%	0.749	0.44	0.51	0.439	−0.04	0.30	0.681
Site 3	1.55	1.82	0.878	25.0%	31.6%	0.851	0.13	0.28	0.504	−0.03	0.27	0.730

$\log_{10}N_w$ along the vertical is lower when compared with that of R. This fact has an impact on the dependency of the performance of radar DSD and rain retrieval algorithms that assume uniform DSD within a radar sampling volume (Gorgucci and Baldini 2015).

c. *MRR–APU comparison*

The 2D histograms between the variables obtained from REP MRR DSDs at 105 m AGL and the ones computed from APU DSD in the three sites considering all the coincident rainy minutes have a similar trend as in Fig. 5 (not shown). The differences between the quantitative comparison presented in Table 5 and the similar statistics presented in Table 3 can be partially ascribed to the fact that the APU underestimates the small drops more than the 2DVD and has a large uncertainty in determining the size of raindrops due to a bin width of 0.5 mm for drops larger than 2.5 mm and of 1.0 mm for drops larger than 5 mm. Furthermore, the sampling cross-sectional area of APU is approximately half that of 2DVD. The absolute biases of Z are relatively larger when APU is compared with MRR's lowest reliable gate for all stratiform and convective rain samples at all sites. The biases of Z are also larger at sites 2 and 3 in stratiform rain. The quantization effect of APU seems to play an important role for these larger biases. The drops larger than 2.5 mm could highly contribute to the reflectivity (Figs. 4c,f,i,l) and it is expected that drops are skewed toward smaller-size drops of the given size bin. Marzuki et al. (2010) showed a drastic increase in the moments of the DSD when the 2DVD drop-by-drop raw data were binned from 0.2 to 0.5 mm. Although outside the scope of this study, we rearranged the 2DVD raw output with APU size intervals. The reflectivity recalculated from simulated APU data was higher by 0.16 dB on average, but the maximum difference in reflectivity between the simulated APU and original 2DVD was 1.9 dB. The quantization effect, of course, is not the sole source of the difference between the APU and 2DVD-based reflectivity. The negative and positive biases of Z in MRR-APU and MRR-2DVD comparisons in site 3, respectively, do not depend on the quantization errors but on the different instrumental error of the two devices. The absolute biases of R were larger, with one exception, in MRR/APU comparison for all the coincident, stratiform and convective rain samples at all three sites (Table 5).

Because 2DVD is more expensive than MRR and APU, a number of field campaigns [e.g., the In-Cloud Icing and Large-Drop Experiment (ICICLE); Bernstein et al. 2018] and field study sites (e.g., that at the National Weather Service Weather Forecast Office at Marquette, Michigan, in support of the GPM mission) have incorporated MRR and APU, but not 2DVD. Also, in this case, the results obtained comparing APU and AVE MRR data are quite close to those obtained comparing APU and REP MRR data for all rain and stratiform rain (Table 5), indicating that, in these conditions, the Adirosi et al. (2016) postprocessing does not produce a significant improvement of the MRR data. Conversely, improvements are evident for convective rain that is, in fact, the main goal of such postprocessing. Table 6 shows results obtained by comparing APU and AVE MRR data during convection. Comparing these results with those in Table 5 for the convective rain, it is clear that the performance of MRR increases using the Adirosi et al. (2016) postprocessing since the statistics in Eqs. (6)–(9) are lower than in Table 6, while the correlations are higher, especially for the reflectivity factor.

Last, as for the comparison between 2DVD and MRR, the bias obtained by comparing APU and MRR increases with height while the correlation coefficient decreases (not shown). The magnitude of the increment

TABLE 6. As Table 4, but for the comparison between APU and MRR (AVE) (number of samples: 120, 255, and 47 for sites 1, 2 and 3, respectively).

	Z (dBZ)			R (mm h^{-1})			D_{mass} (mm)			$\text{Log}_{10}[N_w$ (mm^{-1} m^{-3})]		
	Bias	Abs bias	Corr	Bias	Abs bias	Corr	Bias	Abs bias	Corr	Bias	Abs bias	Corr
Site 1	3.97	4.50	0.532	30.9%	46.9%	0.519	0.55	0.62	0.251	−0.29	0.43	0.686
Site 2	6.86	6.94	0.400	56.1%	58.7%	0.703	0.58	0.63	0.224	−0.08	0.32	0.655
Site 3	4.72	5.02	0.493	45.6%	48.4%	0.709	0.44	0.53	0.086	−0.14	0.36	0.610

and decrement are similar to the ones obtained by comparing 2DVD and MRR. However, in this case, as also stated above, the MRR at site 3 overestimates Z and R with respect to APU.

6. MRR–NPOL radar comparison

In this section, Z_h and Z_{dr} measured by NPOL are compared with those estimated from REP MRR DSD using the T-matrix electromagnetic model (Barber and Yen 1975). Starting from the MRR DSDs obtained every 1 min in each MRR layer, a T matrix was implemented to obtain the Z_h and Z_{dr} at S band assuming a temperature of 20°C, radar elevation angle of 0° (very close to the actual NPOL elevation angles considered so that differences in Z_h and Z_{dr} are negligible), raindrop shape model of Beard and Chuang (1987), and Gaussian canting angle distribution with a mean of 0° and a standard deviation of 10°. In simulating radar measurements, we assume that only raindrops are present in the radar sampling volume. Since this study evaluates the accuracy of MRR, NPOL is a reference instrument and the comparative study was conducted only for radar measurements (Z_h and Z_{dr}) and not radar retrieved products such as DSD parameters and rain rate. A comparison of rainfall rates estimated from NPOL measurements with those computed from APU DSD collected during IFloodS can be found in Chen et al. (2017).

Because of radar beam geometry, the farther the distance from the radar site is, the wider is the radar sampling volume (the latter increases with the square of the range) and the greater the height of the radar beam center from the ground will be. Table 1 shows the height of the NPOL beam center above the three sites. In the NPOL–MRR comparison we considered that, as a result of the beam broadening, the number of MRR range bins within the NPOL measurement volume changes as a function of the distance of the MRR from the radar. To match measurements, we used a beam-weighting function that assigns a different weight at each MRR range bin depending on the distance from the radar site, the radar elevation angle and the antenna radiation pattern assumed to follow a Gaussian shape. The following equations have been adopted (Gorgucci and Baldini 2015):

$$Z_{h,w} = 10\log_{10}\left(\sum_{j=3}^{30} \text{WF}_j P_{h,j}\right) \quad \text{and} \tag{10}$$

$$Z_{\text{dr},w} = 10\log_{10}\left(\frac{\sum_{j=3}^{30} \text{WF}_j P_{h,j}}{\sum_{j=3}^{30} \text{WF}_j P_{v,j}}\right), \tag{11}$$

where $P_{h,j}$ and $P_{v,j}$ are the reflectivity factors at horizontal and vertical polarization in mm^6 m^{-3} in the jth MRR bin weighted by radar illumination function (WF$_j$). The subscript w stands for weighted. The index j ranges between 3 and 30 because the first two and the last MRR bins were considered unreliable and therefore not used. Moreover, only complete columns of MRR data were retained for analysis.

Figure 7 shows the 2D histogram between NPOL measurement (x axis) and REP MRR-based variable (y axis) in all rain condition, and Table 7 reports the performance estimators for 1) all rainy minutes, 2) stratiform rain, and 3) convective rain. For sites 1 and 2, the second radar elevation angle was considered. For site 1, radar returns at the lowest elevation seem to be affected by ground clutter and therefore filtered out by the adopted filter (see section 2b). Also for site 2, the behavior of radar variables at the first elevation in the Z_h–Z_{dr} diagram (not shown) looks unlikely for rain, probably due to residual effects of ground clutter from side lobes. For site 3, the MRR-based variables are plotted against the ones of NPOL at the lowest elevation because the radar beam at the second elevation angle is above the highest MRR bin (Fig. 8).

A good agreement between NPOL Z_h and Z_h estimated from REP MRR-derived DSDs is achieved in terms of bias for all sites (Table 7). Sites 1 and 2 present a bit larger bias (~1 dB for all rain condition) with respect to site 3, where the bias is negligible (less than 0.3 dB for all rain conditions). A certain dispersion of data is evident and leads to values of absolute bias around 2–3 dB

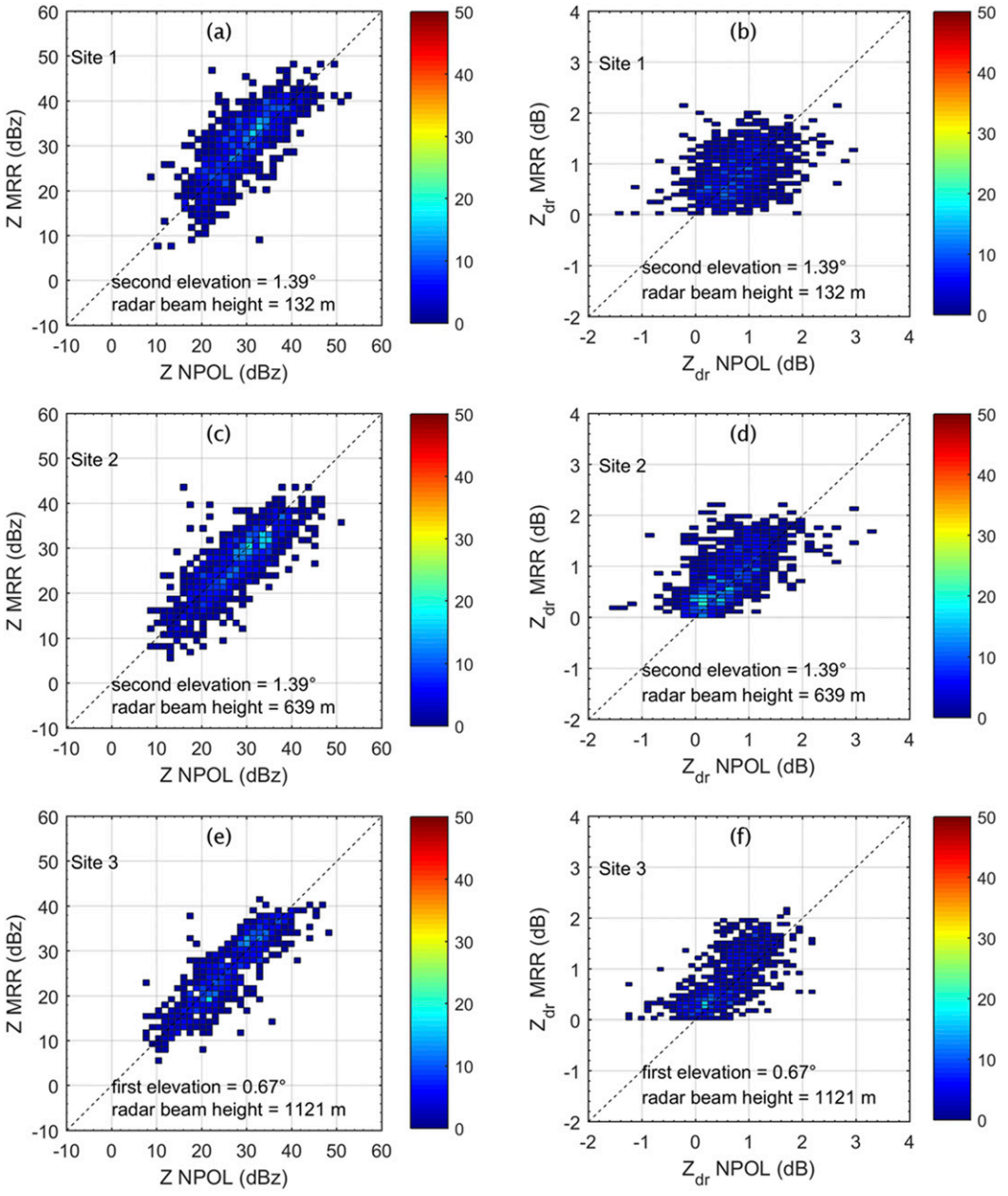

FIG. 7. 2D histograms between (a),(c),(e) the equivalent reflectivity factor at horizontal polarization and (b),(d),(f) differential reflectivity, measured by NPOL (x axis) and the corresponding variables estimated from 1-min DSD obtained by REP MRR data (y axis): comparison of NPOL data from the sweep at the second elevation angle (1.39°) and MRR-based variables at sites (top) 1 and (middle) 2 and(bottom) comparison of MRR-based variables at site 3 with NPOL measurements collected at the first elevation angle (0.67°).

and correlation around 0.8–0.9. For stratiform rain, the absolute bias ranges between 2.78 and 3.57 dB. Tokay et al. (2009) compared MRR and S-band profiled reflectivities, obtaining a bias that ranges between −0.5 and 1 dB. Frech et al. (2017) compared the reflectivity sampled by MRR and by a C-band radar at vertical incidence and obtained a bias (radar less MRR) up to −1.7 dB and a MAD up to 2.5 dB. Please note that in this study the PPIs at low elevation angles are used for comparison purposes and that beam broadening makes the NPOL beamwidth above the three sites 85, 430, and 1200 m. Considering differential reflectivity, a good agreement is obtained between MRR and NPOL, highlighted by the small bias and absolute bias at all the considered sites.

TABLE 7. Performance of the comparison of NPOL measurements and the REP MRR-based variables.

	Z_h (dBZ)			Z_{dr} (dB)		
	Bias	Abs bias	Corr	Bias	Abs bias	Corr
NPOL vs REP MRR—all minutes (no. of samples: 934, 1039, 884 for sites 1, 2 and 3, respectively)						
Site 1	−0.95	3.68	0.782	−0.02	0.43	0.401
Site 2	1.11	3.50	0.814	−0.19	0.37	0.613
Site 3	0.26	2.78	0.878	−0.20	0.36	0.698
NPOL vs MRR REP—Stratiform minutes (no. of samples: 790, 984, 817 for sites 1, 2 and 3, respectively)						
Site 1	−0.66	3.57	0.741	−0.01	0.42	0.381
Site 2	1.03	3.45	0.795	−0.19	0.37	0.593
Site 3	0.27	2.78	0.862	−0.21	0.36	0.689
NPOL vs MRR REP—Convective minutes (no. of samples: 70, 31, 31 for sites 1, 2 and 3, respectively)						
Site 1	−3.21	5.25	0.400	0.01	0.46	0.334
Site 2	3.37	5.41	−0.046	−0.13	0.37	0.424
Site 3	2.08	3.19	0.737	−0.10	0.45	0.415

However, a dispersion of the data around the 1:1 line results in correlations ranging between 0.40 and 0.69. It is important to underline that the assumptions adopted in the T-matrix simulation to obtain radar measurements from MRR DSDs avoid negative values of Z_{dr}, while NPOL measurements also report some negative values of Z_{dr}, mostly due to signal fluctuation that, in light rain, can imply negative Z_{dr}. As shown in Table 7, the results for the stratiform condition are close to the ones obtained considering all the coincident rainy minutes, while in convection, the Z_h bias becomes more important (around 2–3 dB) with low values of the correlations. The results obtained comparing AVE data with NPOL measurements are very close to the ones shown in Table 7.

7. Conclusions

Vertically pointing radars play an important role in radar-based precipitation estimation by filling in the gap between areal radar and point disdrometer/gauge measurements. In that regard, the cost-effective MRR has the potential to become an operational tool as part of automated surface observing systems in the United States and elsewhere. The IFloodS field campaign provided a unique dataset with which to investigate the performance of the MRR by comparing observations from collocated 2DVD and APU disdrometers as well as NPOL. The design of the field campaign with multiple sites, the instruments' performance with minimum failure during the 2-month-long field campaign, and the fortuitous occurrence of abundant rainfall are three main factors contributing to the rich dataset used for comprehensive analysis. This study focused on the accuracy of MRR-derived Z, R, D_{mass}, and $\log_{10}N_w$ considering 2DVD, APU, and NPOL as references. The study included 1) all rainy minutes, and a subset of 2) stratiform and 3) convective rain minutes. First, a postprocessing was applied to the disdrometer and MRR data (section 2b)

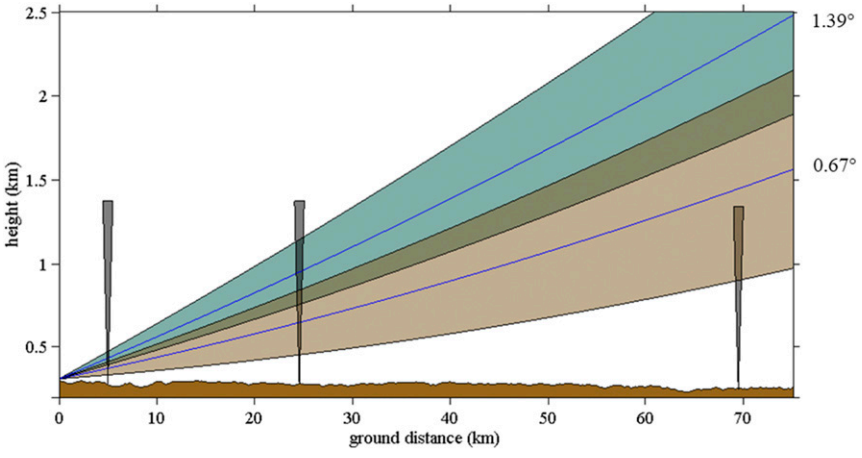

FIG. 8. Geometry of NPOL PPI scanning (only first and second elevation angles are shown) with respect to MRR positioning and maximum height measurements during IFloodS.

to achieve the most reliable disdrometer measurements, extracting contamination of nonmeteorological returns from solid and mixed-phase precipitation, although a nonperfect discrimination could be a caveat. Furthermore, for the MRR an ad hoc postprocessing method developed by Adirosi et al. (2016) was applied to correct the MRR spectra for the effects of vertical wind and, consequently, to obtain more reliable DSD estimates from MRR power spectra, especially during convection.

The DSDs estimated by MRR show different characteristics with respect to those estimated by the disdrometers. For small drops, most MRR DSDs show an upward concavity, whereas 2DVD and APU DSDs exhibit a downward concavity. For large drops, the MRR intrinsic upper limit of 5.03 mm creates discrepancies with the DSD estimated from the disdrometers in convective rain.

The level of agreement between the disdrometers and NPOL with respect to MRR differs from one variable to the next and depends on the sensitivity of the variable to the particular size range and the MRR's ability to retrieve that size range.

Comparing MRR and disdrometers at ground, and considering all the coincident rainy minutes, the absolute bias for Z is almost always less than or around 2 dB for all three sites. The only exception is site 2, where a certain underestimation is obtained by MRR during convective rain. The agreement in terms of rain rate is pointed out by a percent absolute bias that ranges between 28.0% and 36.7% for the comparison of MRR and 2DVD data and reaches greater values when MRR is compared with APU. The agreement in terms of D_{mass} is very good, with absolute bias around 0.2 mm, which is roughly the diameter resolution of 2DVD, while MRR seems to slightly overestimate the number of drops. For convective conditions, the agreement between MRR and 2DVD or APU slightly decreases. However, better results have been obtained when the REP MRR data were used instead of the AVE data. Most of the time, the agreement between 2DVD and MRR at the lowest reliable bin is slightly better than the one between APU and MRR. Finally, comparing the MRR variables at different heights with the ones at ground measured by disdrometers leads to a decrease in the agreement between the instruments. The magnitude of the decrease is an indication of the variability of the precipitation parameters in instantaneous measurements along the vertical, and we found that it highly depends on the choice of variable, in addition to the time–height ambiguity between measurements collected at different heights. In particular, the increment of absolute bias from the lowest to the highest MRR bin is around 100% for the two DSD parameters and higher for the rainfall rate and reflectivity factor. More comprehensive and systematic analysis of the MRR data along the vertical should be done in the future to shed more light on this topic and its implications for applications such as radar retrieval algorithms.

The measurements of MRR along the vertical were also compared with those of NPOL. This was done by simulating vertical profiles of S-band reflectivity factor at horizontal polarization and differential reflectivity from MRR DSDs with T-matrix simulation and properly resampling them onto the NPOL resolution volumes. The agreement in terms of Z_h is very good for all rain conditions, particularly for site 3, with bias equal to 0.26 dB and absolute bias equal to 2.78 dB, whereas for the other two sites bias is around 1 dB and absolute bias is around 3.5 dB. The bias obtained from comparing reflectivity from MRR and NPOL (Table 7) is comparable to that obtained between MRR and 2DVD at ground level (Table 3). However, in the latter comparison a lower absolute bias and higher correlation have been found. Note that the reflectivity used to obtain merit parameters in Table 3 are computed under Rayleigh assumption. The comparison in terms of Z_{dr} shows a larger dispersion of MRR-based data with respect to NPOL measurements, but the result is likely influenced by the assumptions adopted in the T-matrix simulation (such as the type of hydrometeors and the shape–size model). In convection, the agreement is still not very good and in terms of merit parameters is worse than the one obtained at ground level between MRR and 2DVD.

This study revealed that the MRR is a valuable tool in quantitative precipitation estimation from radar remote sensing. Because both disdrometers and MRRs are research tools, we are limited with the field campaign-based datasets that represent certain climate regimes. In this study, central Iowa receives precipitation from frontal systems, mesoscale convective complexes, and airmass thunderstorms during the spring. There is merit in repeating this study at different climate zones, especially at sites where tropical oceanic rainfall occurs. There is also an interest in using MRR in winter precipitation. Similar studies are also desirable at high latitudes. However, further work is needed to improve the accuracy of MRR during convection conditions.

Acknowledgments. This work has been partially supported by the Italian Ministry of University and Research (Project PRIN-20154WX5NA "Reconciling precipitation with runoff: The role of understated measurement biases in the modelling of hydrological processes") and the NASA Precipitation Measurement Mission through Grant NNX16AE88G. The authors acknowledge the NASA GPM mission Ground Validation program for

providing the data of the IFloodS field campaign and, in particular, the GPM Ground Validation Team based at NASA GSFC (Greenbelt, Maryland, and Wallops Flight Facility, Wallops Island, Virginia) for providing support and useful information with regard to NPOL and MRR calibration.

REFERENCES

Adirosi, E., L. Baldini, N. Roberto, P. Gatlin, and A. Tokay, 2016: Improvement of vertical profiles of raindrop size distribution from Micro Rain Radar using 2D video disdrometer measurements. *Atmos. Res.*, **169**, 404–415, https://doi.org/10.1016/j.atmosres.2015.07.002.

Atlas, D., R. C. Srivastava, and R. S. Sekhon, 1973: Doppler radar characteristics of precipitation at vertical incidence. *Rev. Geophys. Space*, **11**, 1–35, https://doi.org/10.1029/RG011i001P00001.

Barber, P. W., and C. Yen, 1975: Scattering of electromagnetic waves by arbitrarily shaped dielectric bodies. *Appl. Opt.*, **14**, 2864–2872, https://doi.org/10.1364/AO.14.002864.

Beard, K. V., and C. Chuang, 1987: A new model for the equilibrium shape of raindrops. *J. Atmos. Sci.*, **44**, 1509–1524, https://doi.org/10.1175/1520-0469(1987)044<1509:ANMFTE>2.0.CO;2.

Bendix, J., R. Rollenbeck, and C. Reudenbach, 2006: Diurnal patterns of rainfall in a tropical Andean valley of southern Ecuador as seen by a vertically pointing K-band Doppler radar. *Int. J. Climatol.*, **26**, 829–846, https://doi.org/10.1002/joc.1267.

Bernstein, B. C., and Coauthors, 2018: ICICLE: Winter 2018–19 In-Cloud Icing and Large-Drop Experiment. *19th Symp. on Meteorological Observation and Instrumentation*, Austin, TX, Amer. Meteor. Soc., 11.3, https://ams.confex.com/ams/98Annual/webprogram/Paper335322.html.

Cha, J. W., K. H. Chang, S. S. Yum, and Y. J. Choi, 2009: Comparison of the bright band characteristics measured by Micro Rain Radar (MRR) at a mountain and a coastal site in South Korea. *Adv. Atmos. Sci.*, **26**, 211–221, https://doi.org/10.1007/s00376-009-0211-0.

Chen, H., V. Chandrasekar, and R. Bechini, 2017: An improved dual-polarization radar rainfall algorithm (DROPS2): Application in NASA IFloodS field campaign. *J. Hydrometeor.*, **18**, 917–937, https://doi.org/10.1175/JHM-D-16-0124.1.

Chen, Y., H. Liu, J. An, U. Görsdorf, and F. H. Berger, 2015: A field experiment on the small-scale variability of rainfall based on a network of Micro Rain Radars and rain gauges. *J. Appl. Meteor. Climatol.*, **54**, 243–255, https://doi.org/10.1175/JAMC-D-13-0210.1.

Das, S., A. K. Shukla, and A. Maitra, 2010: Investigation of vertical profile of rain microstructure at Ahmedabad in Indian tropical region. *Adv. Space Res.*, **45**, 1235–1243, https://doi.org/10.1016/j.asr.2010.01.001.

Fraile, R., A. Castro, M. González-Colino, E. Alonso-Blanco, M. Fernández-Raga, C. Palencia, and A. I. Calvo, 2015: Vertical raindrop size distribution in central Spain: A case study. *Adv. Meteor.*, **2015**, 647647, https://doi.org/10.1155/2015/647647.

Frech, M., M. Hagen, and T. Mammen, 2017: Monitoring the absolute calibration of a polarimetric weather radar. *J. Atmos. Oceanic Technol.*, **34**, 599–615, https://doi.org/10.1175/JTECH-D-16-0076.1.

Giangrande, S. E., E. P. Luke, and P. Kollias, 2012: Characterization of vertical velocity and drop size distribution parameters in widespread precipitation at ARM facilities. *J. Appl. Meteor. Climatol.*, **51**, 380–391, https://doi.org/10.1175/JAMC-D-10-05000.1.

Gorgucci, E., and L. Baldini, 2015: Influence of beam broadening on the accuracy of radar polarimetric rainfall estimation. *J. Hydrometeor.*, **16**, 1356–1371, https://doi.org/10.1175/JHM-D-14-0084.1.

Kirankumar, N. V. P., and P. K. Kunhikrishnan, 2013: Evaluation of performance of Micro Rain Radar over the tropical coastal station Thumba (8.5°N, 76.9°E). *Atmos. Res.*, **134**, 56–63, https://doi.org/10.1016/j.atmosres.2013.07.018.

Kneifel, S., M. Maahn, G. Peters, and C. Simmer, 2011: Observation of snowfall with a low-power FM-CW K-band radar (Micro Rain Radar). *Meteor. Atmos. Phys.*, **113**, 75–87, https://doi.org/10.1007/s00703-011-0142-z.

Kubota, and Coauthors, 2014: Evaluation of precipitation estimates by at-launch codes of GPM/DPR algorithms using synthetic data from TRMM/PR observations. *IEEE J. Sel. Top. Appl. Earth Obs. Remote Sens.*, **7**, 3931–3944, https://doi.org/10.1109/JSTARS.2014.2320960.

Lombardo, F., F. Napolitano, F. Russo, G. Scialanga, L. Baldini, and E. Gorgucci, 2006: Rainfall estimation and ground clutter rejection with dual polarization weather radar. *Adv. Geosci.*, **7**, 127–130, https://doi.org/10.5194/adgeo-7-127-2006.

Maahn, M., and P. Kollias, 2012: Improved Micro Rain Radar snow measurements using Doppler spectra post-processing. *Atmos. Meas. Tech.*, **5**, 2661–2673, https://doi.org/10.5194/amt-5-2661-2012.

Maddox, R. A., J. Zhang, J. J. Gourley, and K. W. Howard, 2002: Weather radar coverage over the contiguous United States. *Wea. Forecasting*, **17**, 927–934, https://doi.org/10.1175/1520-0434(2002)017<0927:WRCOTC>2.0.CO;2.

Marzuki, M., W. L. Randeu, M. Schönhuber, V. N. Bringi, T. Kozu, and T. Shimomai, 2010: Raindrop size distribution parameters of disdrometer data with different bin sizes. *IEEE Trans. Geosci. Remote Sens.*, **48**, 3075–3080, https://doi.org/10.1109/TGRS.2010.2043955.

Peters, G., B. Fischer, H. Münster, M. Clemens, and A. Wagner, 2005: Profiles of raindrop size distributions as retrieved by microrain radars. *J. Appl. Meteor.*, **44**, 1930–1949, https://doi.org/10.1175/JAM2316.1.

——, ——, and M. Clemens, 2010: Rain attenuation of radar echoes considering finite-range resolution and using drop size distributions. *J. Atmos. Oceanic Technol.*, **27**, 829–842, https://doi.org/10.1175/2009JTECHA1342.1.

Petersen, W., and W. Krajewski, 2013: Status update on the GPM Ground Validation Iowa Flood Studies (IFloodS) field experiment. *Geophysical Research Abstracts*, Vol. 15, Abstract 13345, http://meetingorganizer.copernicus.org/EGU2013/EGU2013-13345.pdf.

——, A. Tokay, P. N. Gatlin, and M. T. Wingo, 2014a: GPM Ground Validation two-dimensional video disdrometer (2DVD) IFloodS. NASA Global Hydrology Resource Center DAAC, accessed July 2016, https://doi.org/10.5067/GPMGV/IFLOODS/2DVD/DATA301.

——, ——, ——, and ——, 2014b: GPM Ground Validation Autonomous Parsivel Unit (APU) IFloodS. NASA Global Hydrology Resource Center DAAC, accessed July 2016, https://doi.org/10.5067/GPMGV/IFLOODS/2DVD/DATA301.

——, P. N. Gatlin, and M. T. Wingo, 2015: GPM Ground Validation Micro Rain Radar (MRR) NASA IFloodS. NASA Global Hydrology Resource Center DAAC, accessed July 2016, https://doi.org/10.5067/GPMGV/IFLOODS/2DVD/DATA301.

Pippitt, J. L., D. B. Wolff, W. Petersen, and D. A. Marks, 2015: Data and operational processing for NASA's GPM Ground Validation program. *37th Conf. on Radar Meteorology*, Norman, OK,

Amer. Meteor. Soc., 111, https://ams.confex.com/ams/37RADAR/webprogram/Paper275627.html.

Prat, O. P., and A. P. Barros, 2010: Ground observations to characterize the spatial gradients and vertical structure of orographic precipitation—Experiments in the inner region of the Great Smoky Mountains. *J. Hydrol.*, **391**, 141–156, https://doi.org/10.1016/j.jhydrol.2010.07.013.

Schönhuber, M., G. Lammer, and W. L. Randeu, 2007: One decade of imaging precipitation measurement by 2D-video-disdrometer. *Adv. Geosci.*, **10**, 85–90, https://doi.org/10.5194/adgeo-10-85-2007.

Schuur, T. J., H. S. Park, A. V. Ryzhkov, and H. D. Reeves, 2012: Classification of precipitation types during transitional winter weather using the RUC model and polarimetric radar retrievals. *J. Appl. Meteor. Climatol.*, **51**, 763–779, https://doi.org/10.1175/JAMC-D-11-091.1.

Seo, B.-C., and Coauthors, 2018: Comprehensive evaluation of the IFloodS radar rainfall products for hydrologic applications. *J. Hydrometeor.*, **19**, 1793–1813, https://doi.org/10.1175/JHM-D-18-0080.1.

Thurai, M., and V. N. Bringi, 2018: Application of the generalized gamma model to represent the full rain drop size distribution spectra. *J. Appl. Meteor. Climatol.*, **57**, 1197–1210, https://doi.org/10.1175/JAMC-d-17-0235.1.

——, ——, and P. T. May, 2010: CPOL radar-derived drop size distribution statistics of stratiform and convective rain for two regimes in Darwin, Australia. *J. Atmos. Oceanic Technol.*, **27**, 932–942, https://doi.org/10.1175/2010JTECHA1349.1.

——, K. V. Mishra, V. N. Bringi, and W. F. Krajewski, 2017: Initial results of a new composite-weighted algorithm for dual-polarized X-band rainfall estimation. *J. Hydrometeor.*, **18**, 1081–1100, https://doi.org/10.1175/JHM-D-16-0196.1.

Tokay, A., A. Kruger, and W. F. Krajewski, 2001: Comparison of drop size distribution measurements by impact and optical disdrometers. *J. Appl. Meteor.*, **40**, 2083–2097, https://doi.org/10.1175/1520-0450(2001)040<2083:CODSDM>2.0.CO;2.

——, P. Hartmann, A. Battaglia, K. S. Gage, W. L. Clark, and C. R. Williams, 2009: A field study of reflectivity and *Z*–*R* relations using vertically pointing radars and disdrometers. *J. Atmos. Oceanic Technol.*, **26**, 1120–1134, https://doi.org/10.1175/2008JTECHA1163.1.

——, W. A. Petersen, P. Gatlin, and M. Wingo, 2013: Comparison of raindrop size distribution measurements by collocated disdrometers. *J. Atmos. Oceanic Technol.*, **30**, 1672–1690, https://doi.org/10.1175/JTECH-D-12-00163.1.

——, D. B. Wolff, and W. A. Petersen, 2014: Evaluation of the new version of the laser-optical disdrometer, OTT Parsivel^2. *J. Atmos. Oceanic Technol.*, **31**, 1276–1288, https://doi.org/10.1175/JTECH-D-13-00174.1.

Tridon, F., J. Van Baelen, and Y. Pointin, 2011: Aliasing in Micro Rain Radar data due to strong vertical winds. *Geophys. Res. Lett.*, **38**, L02804, https://doi.org/10.1029%2F2010GL046018.

Wen, L., K. Zhao, G. Zhang, M. Xue, B. Zhou, S. Liu, and X. Chen, 2016: Statistical characteristics of raindrop size distributions observed in East China during the Asian summer monsoon season using 2D video disdrometer and Micro Rain Radar data. *J. Geophys. Res. Atmos.*, **121**, 2265–2282, https://doi.org/10.1002/2015JD024160.

Williams, C. R., 2002: Simultaneous ambient air motion and raindrop size distributions retrieved from UHF vertical incident profiler observations. *Radio Sci.*, **37**, 1024, https://doi.org/10.1029/2000RS002603.

Wingo, S. M., W. A. Petersen, P. N. Gatlin, C. S. Pabla, D. A. Marks, and D. B. Wolff, 2018: The System for Integrating Multiplatform Data to Build the Atmospheric Column (SIMBA) precipitation observation fusion framework. *J. Atmos. Oceanic Technol.*, **35**, 1353–1374, https://doi.org/10.1175/JTECH-D-17-0187.1.

Wolff, D. B., D. A. Marks, and W. A. Petersen, 2015a: GPM Ground Validation NASA S-band dual polarimetric (NPOL) Doppler radar IFloodD V2. NASA Global Hydrology Resource Center DAAC, accessed July 2016, https://doi.org/10.5067/GPMGV/IFLOODS/NPOL/DATA102.

——, ——, and ——, 2015b: General application of the relative calibration adjustment (RCA) technique for monitoring and correcting radar reflectivity calibration. *J. Atmos. Oceanic Technol.*, **32**, 496–506, https://doi.org/10.1175/JTECH-D-13-00185.1.

Zhang, J., and Coauthors, 2016: Multi-Radar Multi-Sensor (MRMS) quantitative precipitation estimation: Initial operating capabilities. *Bull. Amer. Meteor. Soc.*, **97**, 621–638, https://doi.org/10.1175/BAMS-D-14-00174.1.